UC Berkeley
UC Berkeley Previously Published Works

Title

Iron-rich microstructure records of high temperature multi-component silicate melt behavior in nuclear fallout

Permalink

https://escholarship.org/uc/item/8kg095vk

Authors

Genda, Tim
Knight, Kim
Dai, Zurong R
et al.

Publication Date

2021-10-01

DOI

10.1016/j.jenvrad.2021.106700

Peer reviewed

Iron-rich microstructure records of high temperature multi-component silicate melt behavior in nuclear fallout

Tim Genda[a,*], Kim Knight[b], Zurong R. Dai[b], Enrica Balboni[b], Bethany L. Goldblum[a,c] and Peter Hosemann[a]

[a]Department of Nuclear Engineering, University of California, Berkeley, USA
[b]Lawrence Livermore National Laboratory, Livermore, USA
[c]Lawrence Berkeley National Laboratory, Berkeley, USA

ABSTRACT

Above-ground nuclear explosions that interact with the surface of the earth entrain materials from the surrounding environment, influencing the resulting physical and chemical evolution of the fireball, which can affect the final chemical phase and mobility of hazardous radionu-clides that are dispersed in the environment as fallout particles. The interaction of iron with a nuclear explosion is of specific interest due to the potential for iron to act as a redox buffer and because of the likelihood of significant masses of metals to be present in urban environments. We investigated fallout from a historic surface interacting nuclear explosion conducted on a steel tower and report the discovery of widespread and diverse iron-rich micro-structures pre-served within the samples, including crystalline dendrites and micron-scale iron-rich spheres with liquid immiscibility textures. We assert these micro-structures reflect local redox con-ditions and cooling rates and can inform interpretation of high temperature events, enabling new insights into fireball condensation physics and chemistry when metals from the local environment (i.e. structural steel) are vaporized or entrained. These observations also signifi-cantly expand the availability of silicate immiscibility datasets applicable to rapidly quenched systems such as meteorite impact melt glass.

1. Introduction

In an above-ground, near-surface nuclear explosion, energy is released that can be millions of times more powerful than the largest conventional explosion, vaporizing both the device and surrounding material and forming a fireball that rises and cools in a matter of seconds (Glasstone et al., 1977). As the vapor condenses, additional proximate material may be entrained, creating fallout particles that are a mixture of environmental materials and condensed bomb vapor (Adams et al., 1960; Freiling et al., 1965). An understanding of how the cooling rate and fireball chemistry fractionates radionuclides during this process is necessary for predictions of fallout distributions used in preparing for and responding to nuclear explosions (Freiling, 1961; Nathans et al., 1970; Storebö, 1960; Crocker et al., 1965; Norman and Winchell, 1966; Miller, 1960; Freiling and Kay, 1966; Storebo, 1974) and for models of radionuclide environmental transport (Lukashenko et al., 2020; Kersting et al., 1999). The extent to which variations in local environments may influence cooling and chemistry behavior in fireballs remains ill constrained.

Current fallout formation models are semi-empirical and based on observations from above-ground nuclear weapons testing and compositional analysis of fallout in the 1940s-1960s representing a limited range of environments (Glasstone et al., 1977; Adams et al., 1960; Freiling et al., 1965; Freiling, 1961; Nathans et al., 1970; Storebö, 1960). Such models assume a homogeneous, fully oxygenated fireball (Freiling, 1961; Nathans et al., 1970; Storebö, 1960), and largely ignore differences in the local settings of the nuclear event. Recent efforts applying modern tools to re-investigate historic fallout (Eby et al., 2015; Cassata et al., 2014; Bonamici et al., 2017; Pacold et al., 2016; Lewis et al., 2015; Weisz et al., 2018; Bellucci and Simonetti, 2012) challenge many fallout formation assumptions with
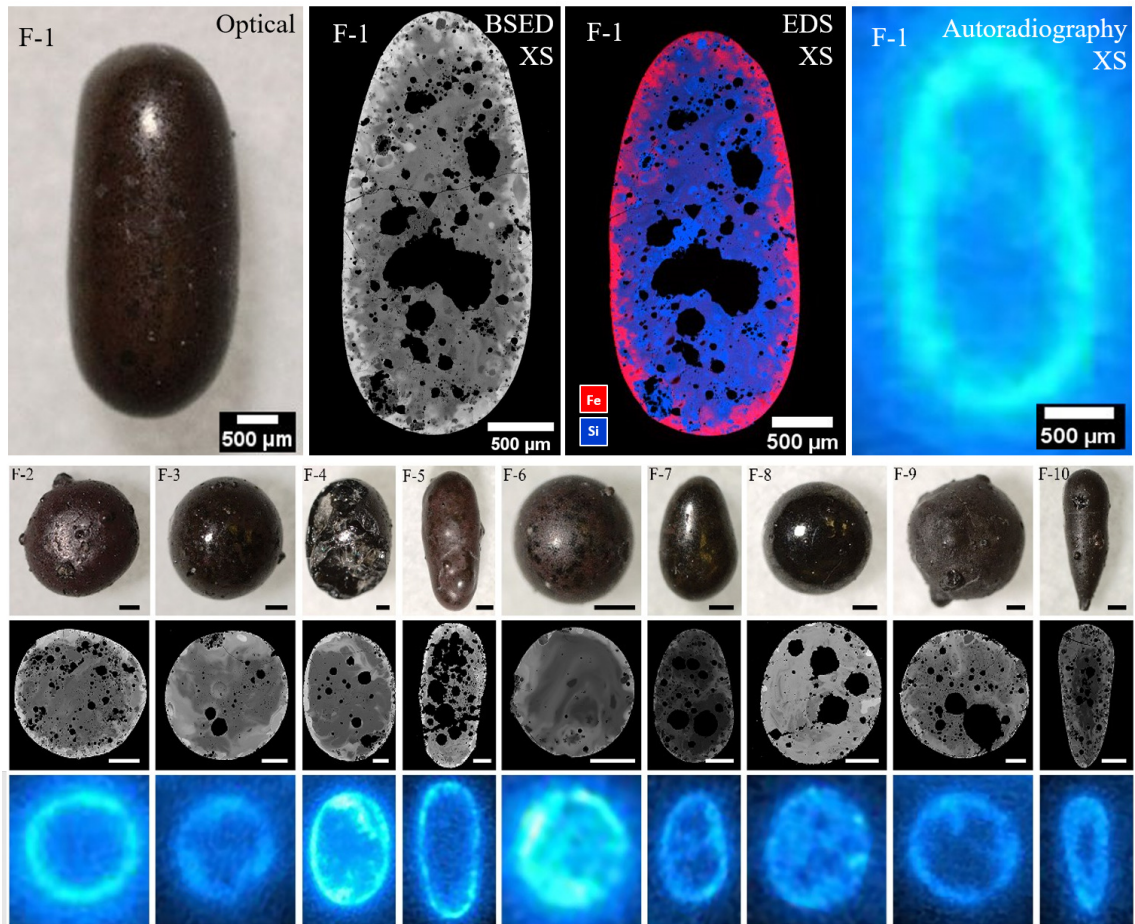
Figure 1: Overview of ten iron-rich aerodynamic fallout samples investigated in this study: The top row displays an optical image of F-1, an exposed cross section backscatter electron detection (BSED) image, an exposed cross section energy dispersive x-ray spectroscopy (EDS) map of Fe and Si, and exposed cross section autoradiography. In these samples, BSED brightness corresponds most strongly to higher iron concentration, as shown by EDS mapping of sample F-1. Each BSE image is contrast adjusted, so comparisons of iron concentration should not be made between images. Pixel brightness in autoradiography images correspond to relative alpha and beta radioactivity. Because all radiographs were collected in a single exposure, relative intensities are comparable between samples. Optical, BSED and autoradiography images of samples F-2 through F-10 are shown in the bottom three rows, and EDS maps showed similar correlations between Fe concentration and BSED contrast. Note the strong correlation between regions of high iron content and radioactivity. No positive correlation between radioactivity was observed for any other major elements in the samples. All scale bars are 500 µm.

evidence of reduced conditions (Cassata et al., 2014; Bonamici et al., 2017; Pacold et al., 2016), heterogeneous vapors (Lewis et al., 2015), and unexpected volatility behavior (Weisz et al., 2018)), motivating research into how and to what extent entrained materials may influence the fireball environment, affecting chemical speciation and partitioning during fallout formation. The interaction of iron with a nuclear explosion is of specific interest on account of the potential for iron to act as a mineral redox buffer (Myers and Eugster, 1983) affecting the chemical behavior of condensing radioactive species (Cassata et al., 2014) and because of the likely presence of masses of metals in the case of an explosion in an urban environment.

The record of high temperature system dynamics preserved in fallout shares similarities with and thus can also assist in understanding other high temperature processes such as planetary formation in the early solar system (Day et al., 2017; Bonamici et al., 2017), meteorite impacts and tektite formation, (Bunch et al., 2012; Glass et al., 1987)), lightning strike fulgurite glass (Essene and Fisher, 1986; Pasek and Pasek, 2018), lunar glass (Roedder and Weiblen, 1970) and terrestrial magmatic systems (Kamenetsky et al., 2013; Veksler et al., 2007). In particular, cratering mete-

orite impact events mix impactor and target lithologies (Osinski et al., 2008; Grieve and Pesonen, 1996) resulting in complex melt evolution (Hamann et al., 2018; Osinski, 2003) which cools at similar rates as nuclear fireball systems (10s-100s K/sec) (Cassata et al., 2014; Weisz et al., 2018; Ebert et al., 2017). While terrestrial cratering impact events have never been directly observed (Grieve and Pesonen, 1996), fallout from nuclear testing formed under relatively well-documented conditions (Glasstone et al., 1977; Adams et al., 1960; Freiling, 1961; Freiling et al., 1965; Nathans et al., 1970; Storebö, 1960; Lukashenko et al., 2020; Kersting et al., 1999; Eby et al., 2015; Cassata et al., 2014; Bonamici et al., 2017; Pacold et al., 2016; Lewis et al., 2015; Weisz et al., 2018; Bellucci and Simonetti, 2012) and thus offers the potential for comparative composition, thermal, and kinetic constrains on formation processes within the resulting melts.

If a nuclear detonation occurs that vaporizes or entrains silicate minerals and additional iron (such as a structural tower or nearby buildings), the resulting fallout has the potential to result in compositions that are sufficiently enriched in iron (several weight percent or more) to fall within a stable two-liquid immiscibility field. Immiscible liquids generally have the potential to be present for some melt compositions and temperatures in glass-forming iron-rich aluminosilicate systems, where varying structural roles of cation species in the melt result in stable silicate-rich liquids (L_{Si}) and iron-rich liquids (L_{Fe}) (Thompson et al., 2007; Hudon and Baker, 2002). Previous studies of mm-scale trinitite glass formed in the first nuclear explosion have noted the presence of metal or metal oxide species and limited textural evidence of liquid immiscibility (Bunch et al., 2012; Eby et al., 2015; Bellucci and Simonetti, 2012). However, such observations and interpretations have remained sparse, likely because thermodynamically stable immiscible liquids only exist for a limited range of compositions, oxygen environments, and temperatures. The compositional and temperature range of this field is sensitive to the species present in the melt, as well as the oxygen fugacity (fO_2) of the system (Naslund, 1983). Thus, the extent to which liquid immiscibility is present in systems where two phase immiscible compositions are stable has the potential to constrain the fO_2 and temperature history of the fireball, and further our understanding of how and to what degree fallout formation processes differ according to local environment. In addition, liquid phase separation affects nearly all the properties of glass, and tends to decrease the chemical durability of the glass, which may result in increased radionuclide mobility in glasses where this process is significant (Weber et al., 1997).

Here, we report the widespread occurrence of novel iron-rich micro-structures, some of which likely are formed as a result of liquid-liquid immiscibility processes, preserved in the rims of aerodynamic fallout glass. These micro-structures significantly expand on previous fallout observations with unique morphology observations and a wider prevalence and diversity of immiscible textures and micro-structures. Some micro-structure morphologies and locations within the mm-scale glass suggests immiscible phase formation outside the glass (*ex situ*) as micro-scale droplets that later agglomerated, and thus more directly reflect the local vapor environment than previous liquid immiscibility observations. Such *ex situ* formation processes suggest understanding liquid immiscibiltiy behavior in fallout, and more broadly in rapidly quenched systems, may be more important to understanding complex fallout formation conditions in iron-rich environments than previously recognized.

2. Materials and Methods

Samples of mm-scale nuclear fallout samples were isolated from soil samples collected near the detonation sites of historic near-surface nuclear weapons tests. Ten individual specimens with spherical or teardrop aerodynamic morphologies and with red or black surface color which have been historically associated with iron content in fallout were selected for analysis. Specimens were optically characterized, carbon coated, and imaged using a FEI Inspect F Scanning Electron Microscope (SEM) at 20 kV using secondary electron detection to investigate surface morphologies and backscatter electron detection (BSED) to identify surface micro-structures. Specimens were then mounted in eponate araldite epoxy in stainless steel round mounts and hand-polished to expose approximate mid-plane cross sections to a 1 μm surface roughness using a range of sandpaper grits, 3 μm and 1 μm diamond paste, and 1 μm alumina powder. Ultrasonication between each step was used to remove residual grit, and exposed vesicles were backfilled with epoxy. Sample pucks were placed face-down on a Fujifilm BAS-SR phosphor storage imaging plate and exposed for six hours to detect alpha and beta radiation using the procedure of (Parsons-Davis et al., 2018). A carbon coat was applied to the exposed cross section prior to BSED imaging of specimen cross sections and micro-structures. Qualitative SEM Energy Dispersive X-ray Spectroscopy (SEM-EDS) maps were taken of the entire exposed mid-plane on some specimens of interest using 1-hour raster across each exposed cross section. EDS data confirms that BSE contrast is most sensitive to local variations in iron concentration.

Qualitative compositional maps of amoeoboids were used to understand the general partitioning behavior of elements between the two phases present in amoeboid micro-structures. Semi-quantitative raster EDS analyses over exposed amoeboid cross sections were used to approximate the average compositions of individual amoeboids, and 10 L_{Si} and 10 L_{Fe} point spectra were taken in different locations at 10 keV within the amoeboid to approximate compositions of each phase. Lower beam energies of 10 kV were used for spot analyses to minimize the excitation volume and obtain compositional measurements for regions on the spatial scale of the approximate matrix excitation volume (1 μm). Because the size of the L_{Si} features is typically on the scale of the approximate excitation volume of the electron beam in the matrix, electron-beam mixing may exist between analyses of the L_{Si} and L_{Fe} phases. This effect would result in overestimation of iron content in the L_{Si} phase or underestimation of iron content in the L_{Fe} phase. However, using an electron beam of 10 keV, the Fe Kα X-ray at an energy of 6.5 keV should produce X-rays from a depth of 0.7 μm according to the Anderson-Hasler range equation, which is less than the domain size of most L_{Si} phases analyzed, minimizing the impact of electron beam mixing. Bulk and two-phase composition estimations shown in the appendix all are consistent with silicate immiscibility as expressed as a pseudo-ternary Greig diagram often used to plot and compare immiscible systems. If compositional contrast is underestimated due to electron beam mixing effects, then true compositions reflect wider miscibility gaps.

Transmission electron microscopy (TEM) of one amoeboid region was conducted using a FEI Titan STEM/TEM located at Lawrence Livermore National Laboratory and was operated at 300 keV. The TEM foil was prepared using a FEI Helios 600i Dual Beam FIB-SEM at Lawrence Livermore National Laboratory. A Pt protective coating was deposited on the surface sample, and a Ga+ ion beam was used to sputter trenches on each side of the planned amoeboid cross section. An OmniProbe sample lift-out system was then used to lift out the cross section and mount it on a TEM half-moon copper grid, which was then thinned to sufficient thickness using the Ga+ ion source (100 nm) for TEM analysis. Images of the foil were taken using bright field and dark field modes, and selected area diffraction patterns were recorded for use in identifying phases present within the foil.

3. Results

Ten aerodynamic glassy fallout samples (F-1 through F-10, 1.5-4 mm in diameter) with reddish-black surfaces of either a dull opaque or glassy luster were collected from historic near-surface nuclear weapons tests involving iron structure. Optical images of each sample, and BSED and autoradiography images of their exposed cross sections are shown in Fig. 1. Polished cross section energy dispersive X-ray spectroscopy (SEM-EDS) and autoradiography (Parsons-Davis et al., 2018) reveal a glassy interior and positive correlation between residual alpha/beta radioactivity and local iron concentrations. No significant positive correlation of radioactivity with other chemical species present in the samples was noted. All sample rims are enriched in iron compared to the estimated local soil composition of 1-3 wt% FeO (Eppich et al., 2014), with varying level of mixing into iron-poor silicate glass interiors exhibiting varying degrees of vesiculation.

A wide range of micro-structures and textures are abundantly present along the iron-rich radioactive sample rims within 200 μm of sample surfaces, and are described in Fig. 2. The relatively iron-poor interiors lack significant micro-structure and exist primarily as a glass, with evidence of partially molten mineral grains in some samples. Glass and partially molten minerals are consistent with observations of fallout formed from interaction with silicate environments (Bonamici et al., 2017; Pacold et al., 2016; Lewis et al., 2015; Weisz et al., 2018; Bellucci and Simonetti, 2012), but the rim micro-structures significantly deviate from fallout observations in the literature, both in micro-structure prevalence and in morphological diversity. These rim micro-structures and textures consist primarily of interconnected-phase textures, emulsions of iron-rich spheres, nano-scale faceted crystals, and micron-scale dendrite crystals.

Interconnected and emulsion textures range from nanoscale (Figs. 2O, 2Q) to the micron-scale (Figs. 2P, 2R). Interconnected textures consist of networks of iron-rich/silica-poor and iron-poor/silica-rich phase, and emulsion textures consist of iron-rich/silica-poor spheres dispersed in a silicate glass matrix. We use L_{Fe} and L_{Si} to refer to the distinct iron-rich and silica-rich phases present in these textures. The emulsion textures are widespread throughout the iron-rich regions of all sample rims, with local gradations in sphere sizes. Many distinct micron-scale (2-20 μm) iron-rich spheres lacking local gradations and consisting of two distinct L_{Fe} and L_{Si} phases with sharp phase boundaries are concentrated on or near (<50 μm) sample surfaces (Figs 2D-N)). These distinct micro-scale spheres predominantly consist of the minority phase dispersed within the majority phase (Figs. 2D-G), and resemble immiscible amoeboid inclusion textures (Roedder and Weiblen, 1970; Hamann et al., 2018). As such, we
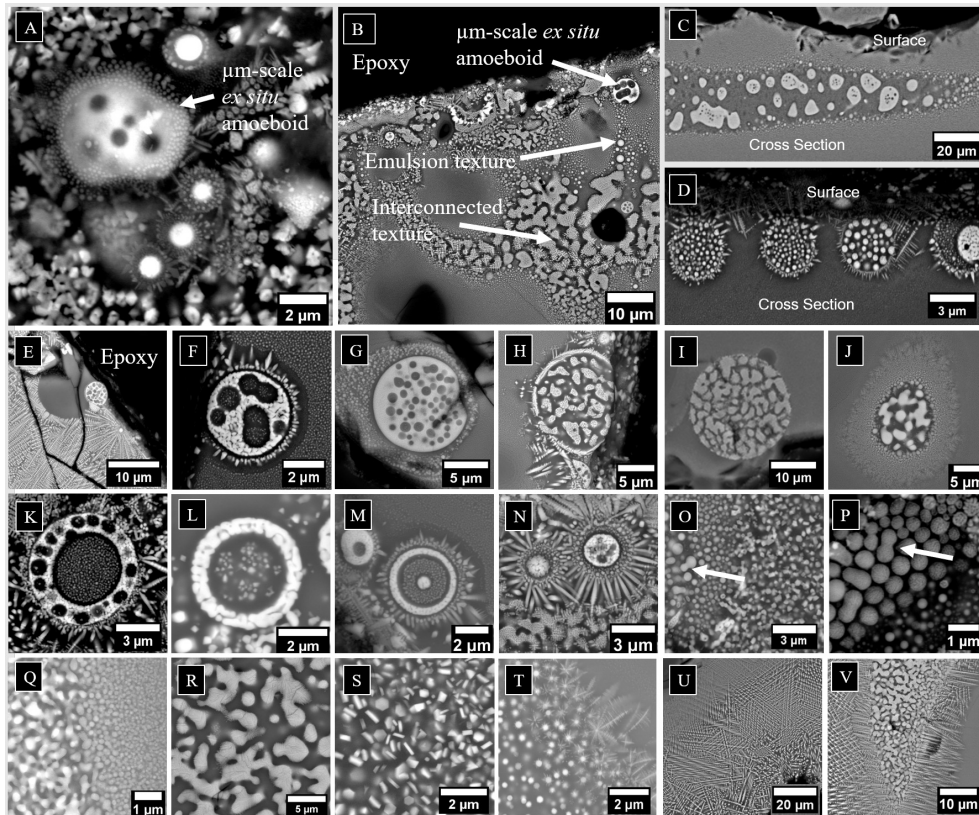
Figure 2: Iron-microstructures of diverse morphologies and prevalence are observed in the iron-rich rims of all samples reported in this study. In all images, brighter pixels correspond to regions of high iron content, where darker pixels unless noted as epoxy) represent more iron-poor, silicate-rich glass. Panel (A) is a surface BSED image of a region of diverse microstructure, whereas panels (B-V) are BSED images taken of the exposed cross sections of samples. (A) and (B) provide examples of regions near sample surfaces with a wide prevalence of emulsion and interconnected textures, *ex situ* amoeboid, and crystalline features. (C) Some regions of immiscible textures characterized by non-spherical morphologies and gradations in emulsion size, likely reflect *in situ* LLPS where iron dissolves into host melts at miscible temperatures before unmixing. Near-surface spherical amoeboid lacking local emulsion gradations likely reflecting ex-situ formation (D-N) are present in all samples. *Ex situ* amoeboid are present in these samples as (D) L_{Fe}-dispersed, (E-G) L_{Si}-dispersed, (H-J) interconnected, and (K-M)core-shell morphologies. The L_{Si}-dispersed amoeboids are most commonly observed. (N) Some amoeboids also exist with radial dendritic crystalline growth features around their exterior. Emulsion textures are present throughout all samples on the (O) nano-scale and (P) μm-scale, with features (white arrows) that suggest merging or splitting of iron-rich droplets. Interconnected textures are also present on the (Q) nanoscale and (R) μm-scale. Crystalline microstructures are also present in the form of (S) nano-scale faceted crystals, (T) dendritic growth nucleated from emulsion textures (U) regions of dendritic growth with individual dendrites as long as 50 microns, and (V) dendritic growth nucleated from interconnected texture regions.

refer to distinct spherical micron-scale two-phase objects as amoeboids in this work to distinguish them from other emulsion and solidification micro-structures. In some cases, amoeboids lack a minority phase dispersion throughout their entire interior, and instead are preserved with interconnected morphologies (Figs. 2H-J), or complex core-shell morphologies (Figs. 2K-M).

Evidence of crystalline growth within samples exists in the form of widespread dendritic magnetite throughout sample rim glass (Figs. 2E, 2U, 2V) reflecting non-equilbrium growth of an iron-oxide phase within the iron-rich silicate melt. In some cases, within the iron-rich silicate rims of the mm-scale samples, dispersions of nanoscale euhedral magnetite crystals are observed (Fig. 2S). Similar magnetite crystals are also observed within the L_{Si} phase of amoeboid structures (Figs. 2F, 2K, 2L, 2M). The L_{Fe} regions of amoeboids sometimes solidify as an apparently single homogeneous phase (Fig. 2G), but usually consist of networks of closely packed non-faceted crystal grains of magnetite in a silicate glass matrix (Figs. 2F, 2L), and occasionally have radial dendritic crystal growth on their
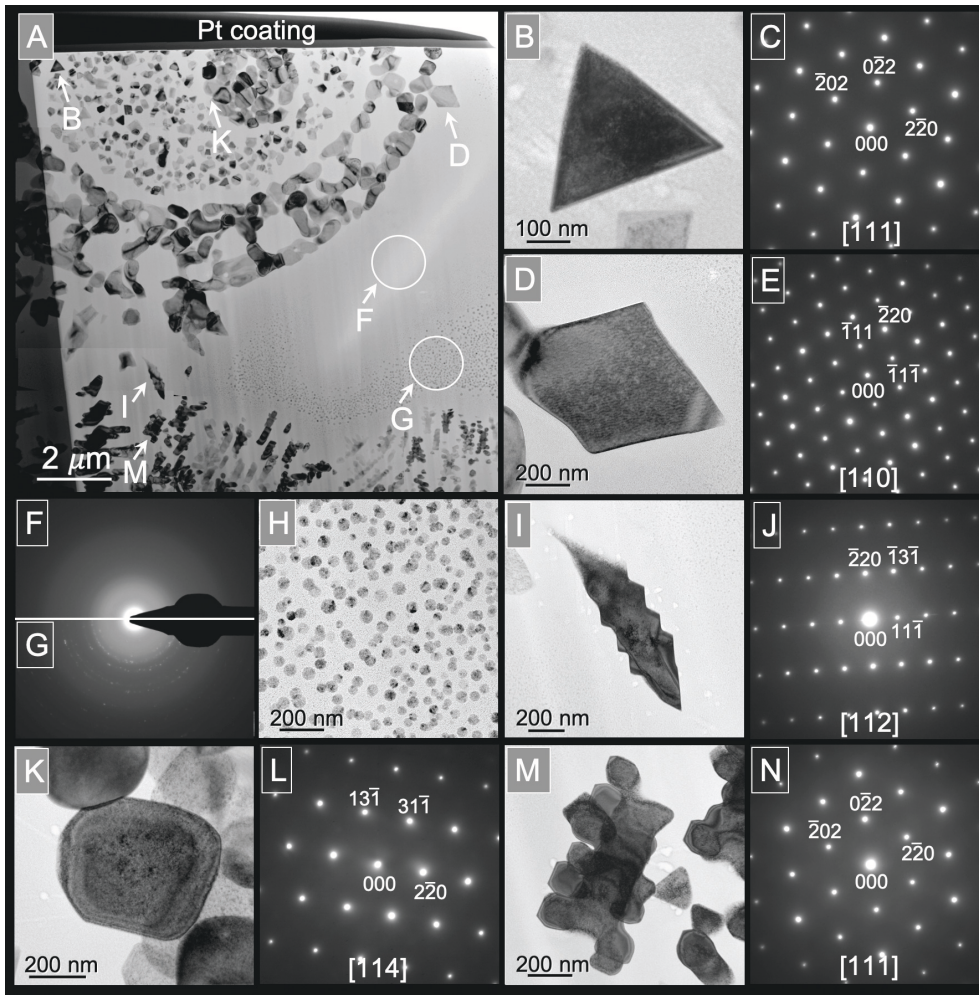
Figure 3: TEM images and electron diffraction patterns of a core-shell amoeboid micro-structure in Sample F-2. (A) Bright-field (BF) image of amoeboid cross-section. (B) BF image of a triangle projection crystal marked by arrowhead B in (A). (C) Selected-area electron diffraction pattern (SADP) of (B). (D) BF image of a diamond projection crystal located in shell (arrowhead D) and its SADP (E). (F) SADP of an iron-poor region (arrowhead F), indicating an amorphous matrix. (G) SADP of a region marked by arrowhead G, indicating an amorphous matrix with crystalline precipitates. (H) An enlarged BF image of the area marked by arrowhead G, showing nano-crystals in an amorphous matrix. (I) BF image of a fusiform shape with bilateral saw-edge projection crystal and its SADP (J). (K) BF image of an equal-axial crystal located in core (arrowhead K) and its SADP (K). (M) BF image of a dendritic crystal outside core-shell amoeboid (arrowhead M) and its SADP (N). All electron diffraction patterns including the ring-pattern (G) match the inverse spinel structured magnetite (Fe3O4: Fd-3m, a = 8.3985 Å)40.

exteriors (Figs. 2M, 2N).

A set of ten amoeboids of similar micro-structure (L_{Si}-dispersed-in-L_{Fe}) were selected for detailed analysis by SEM-EDS, all of which have comparable chemical element compositions (see Appendix) with systematic distributions of elements between the two phases. Assuming standard oxide stoichiometry, the average composition of the selected amoeboids is 40.2 ± 4.3 wt% SiO_2, 48.4 ± 4.3 wt% FeO, 6.1 ± 1.1 wt% Al_2O_3, 1.67 ± 0.22 wt% K_2O, with the remainder composed of MgO, CaO, TiO_2, and Na_2O. The average major element composition of the L_{Fe} phases are 27.0 ± 4.3 wt% SiO_2, 63.3 ± 5.2 wt% FeO, 5.1 ± 1.2 wt% Al_2O_3, 1.1 ± 0.4 wt% K_2O, and of the L_{Si} phases are 61.4 ± 7.3 wt% SiO_2, 23.7 ± 8.5 wt% FeO, 8.1 ± 1.6 wt% Al_2O_3, 3.0 ± 0.6 wt% K_2O. Uncertainties here represent the 1-σ variation between average phase compositions between amoeboids. Species exist in oxide form, but they likely deviate from standard oxide stoichiometry. However, we report results in standard stoichiometry to remain consistent with liquid immiscibility compositional measurements with unknown stoichiometry reported in

the literature (Naslund, 1983; Kamenetsky et al., 2013). Both L_{Fe} and L_{Si} phases are enriched in iron compared to typical silicate soil samples. Transmission electron microscopy (TEM) and electron diffraction analyses of a core-shell amoeboid cross-section from sample F-2 (Fig. 3) confirms the amorphous nature of the L_{Si} glass (Fig. 2F)and that the L_{Fe} regions (Figs. 2D, 2K) crystallize into grains of inverse spinel structured iron-oxide matching magnetite (Fe_3O_4) (Fleet, 1981)). Nano-scale faceted crystals within the L_{Si} regions of amoeboids (Fig. 2B) similar to those dispersed in the host melt (Fig. 1S) and crystals outside the amoeboid (Figs. 2I, 2M) also exhibit the same structure.

4. Discussion

Observed interconnected textures, emulsion textures and amoeboid micro-structures (Fig. 1B-R) are compositionally and texturally consistent with those documented in iron-aluminosilicate liquid immiscible systems (Essene and Fisher, 1986; Roedder and Weiblen, 1970; Roedder, 1978; Veksler et al., 2007). While some textural evidence of liquid immiscibility reported in this work resembles textures reported in trinitite glass formed in the first nuclear explosion (Bunch et al., 2012; Eby et al., 2015), *ex situ* amoeboids significantly deviate from previous immiscibility observations. Their likely *ex situ* formation provides a more direct probe of fireball vapor conditions than previous liquid immiscibility observations. Some *ex situ* amoeboids have concentric layers of L_{Fe} and L_{Si} phases (Fig. 2K, 2L, 2M) which we refer to as "core-shell" amoeboids. These core-shell amoeboids are particularly unique, as they have not been observed in any silicate system, though they resemble micro-structures formed in immiscible metallic alloy microgravity experiments (Shi et al., 2013) or in self-organizing macroscale ternary immiscible systems (Moerman et al., 2018). Some multi-layer core-shell amoeboids with dispersions of a silicate phase within the rim and nano-scale magnetite crystals within their interior (Fig. 3) have not, to our knowledge, been observed in any system, and are unique to iron-rich fallout formation environments.

4.1. Amoeboid Formation Hypothesis

Ex situ LLPS processes are described in the context of conceptual fallout formation models (Glasstone et al., 1977; Adams et al., 1960; Miller, 1960) in Fig. 4. We hypothesize that amoeboids may form first by direct condensation or condensate/melt agglomeration in the vapor at temperatures (>1540 K) (Roedder and Weiblen, 1970) where they exist as a miscible, homogeneous melt droplets. As the droplets and surrounding vapor cools into the liquid immiscible region, they undergo liquid-liquid phase separation (LLPS) into stable compositions reflecting the evolving temperature and redox environments. The temperature range where this occurs will vary depending on the multi-component melt composition of the droplet as well as the local fO_2 conditions, but is 1370-1540 K for the system closest in composition to amoeboids that has been studied(leucite-fayalite-quartz) (Roedder, 1978), though the upper temperature limit increases with fO_2 and varies according to the addition of minor species. After phase separation, amoeboids agglomerate and are subsumed into the airborne, non-vaporized mm-scale host melts sourced from entrained silicate minerals, where they largely preserve their morphologies and compositions prior to the host melt transition to glass. The similarity of core-shell amoeboid morphology to structures formed in other liquid immiscible systems (Moerman et al., 2018; Shi et al., 2013) supports a LLPS process, where immiscible liquid phases coarsen and/or migrate to form self-assembled core-shell structures. This theory is consistent with previous conceptual models of fallout formation and agglomeration for near-surface nuclear detonations, but includes significant (*ex situ*) LLPS processes.

When amoeboids first cool into the miscibility gap and are still far above the liquidus temperature (T_{Liq}), the kinetics of LLPS is very rapid (Ebert et al., 2017). At these temperatures, LLPS may be fast enough to approach equilibrium compositions reflecting the local fO_2 and temperature. As the droplet cools below T_{Liq}, L_{Si} regions then transition to glass and L_{Fe} regions crystallize, preserving interpretable L_{Fe} and L_{Si} compositions within the original liquid phase boundaries reflecting the higher temperature LLPS. However, at temperatures near the liquidus temperature T_{Liq}, the increasingly viscous liquids may be kinetically limited from reaching increasingly contrasting stable equilibrium compositions. Laser melt experiments (Hamann et al., 2018) have shown that LLPS is quite rapid and can occur in less than 0.6-1.4 seconds in silicate systems. Hillendahl cooling curve calculations (Freiling et al., 1965; Klement, 1965) for fireballs result in melt dwell times within the silicate immiscibility temperature range (1370-1540 for the leucite-faylite-silica system) for 1.3 seconds in a 1 kT TNT equivalent explosion, and for 5.1 seconds for a 100 kT TNT equivalent explosion. For high fO_2, the solvus of the immiscibility region will increase, and thus increase the dwell time of the melts within immiscible regions. Thus, it is possible that LLPS may occur rapidly enough to approach equilibrium fO_2-dependent compositions for at least some of the temperature range where
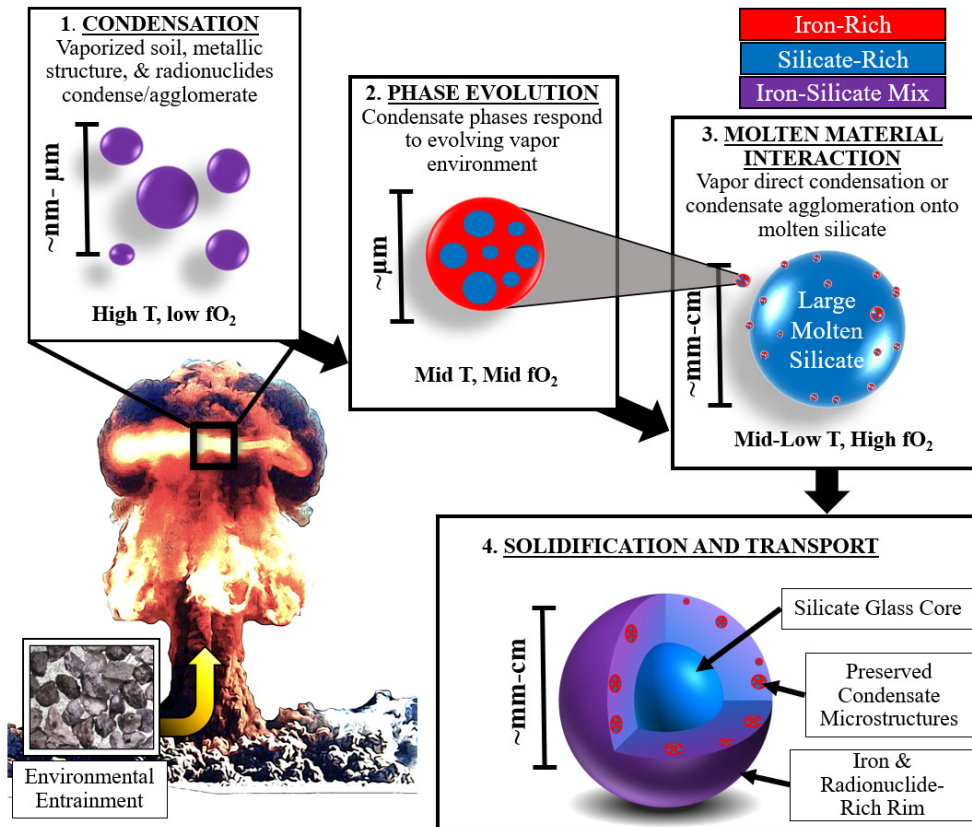
Figure 4: The preservation of immiscible micro-structures in iron- and radioactivity-rich fallout rims reflect vapor conditions for near-surface nuclear explosions in iron-silicate-environments. This graphic depicts the *ex situ* liquid-liquid phase separation (LLPS) in step (2) that led to the development of the complex amoeboid micro-structures that agglomerated onto the molten silicate melts at late times, and are reported in this study in the context of previously described models of mm-scale glassy fallout formation for near-surface nuclear detonations. (Glasstone et al., 1977; Adams et al., 1960; Freiling, 1961; Freiling et al., 1965; Miller, 1960; Storebo, 1974) Condensation and agglomeration can also occur at earlier times and at higher temperatures, where the condensates dissolve into the melt prior to LLPS processes. Such *in situ* LLPS textures are present within the radionuclide, iron-rich rim but with different textural appearance and size distributions than *ex situ* LLPS.

liquid immiscibility occurs.

Oxygen- (Naslund, 1983) and temperature-sensitive (Kamenetsky et al., 2013) thermodynamic approaches to stable liquid immiscibility in multicomponent silicate systems have previously been explored, suggesting amoeboid L_{Fe} and L_{Si} may be sensitive to oxygen fugacity (fO_2) and quench rate. Untangling the effects of each parameter in a quantitative way for fallout conditions is also difficult because amoeboid compositions have minor components that may influence the shape of the immiscibility gap, and because of the uncertainty in LLPS kinetics. However, comparisons to analogous systems are discussed here to offer qualitative constraints, support the theory that they formed via LLPS, and explore whether these micro-structure compositions are sensitive to fireball conditions in a way that may offer independent quantitative constraints in the future. Below, we compare amoeboid compositions to analogous experimental and natural silicate immiscibility data, which supports the hypothesis that amoeboids reflect a sensitive probe of fO_2 and quench rate in iron-rich nuclear fireballs. We compare amoeboid compositions first to data from Naslund (Naslund, 1983), who measured the variations in 2-liquid compositions between stable two-liquid iron-rich silicate pairs for a range of fO_2. In this case, uncertain kinetics allow only a lower bound on fO_2, and remains qualitative due to small deviations in minor components present in the experimental system. We then compare amoeboid compositions to data from Kamenetsky *et al* (Kamenetsky et al., 2013) who explored an empirical correlation between the distribution of SiO_2 between the liquid phases and equilibrium temperature. Significant compositional differences exist that make this comparison qualitative, but we make the argument that,

if the fO_2 is constant during LLPS, variations in the SiO_2 reflect variations in the quench rate, and thus sensitivity to amoeboid thermal histories.

4.2. Amoeboid Record of Oxygen Fugacity

According to traditional fallout models, we assume the after initial heating, reduction, and vaporization, the fireball increases in fO_2 over time due to oxygen entrainment and decreases in temperature due to radiative cooling and environmental entrainment. Both an increase in fO_2 and cooling results in a broadening of the immiscibility gap. If this assumption holds true, this means that, even considering kinetic limitations caused by a rapid quench, any measured compositional contrast between phases represents a lower bound of the local fO_2. Amoeboid bulk compositions are similar in major element composition to the $KAlSi_3O_8 - FeO - Fe_2O_3 - SiO_2$ system liquid immiscibility experiments (Naslund, 1983), with similar two-liquid compositions(Fig. 5). While amoeboids do also include minor amounts of Na_2O, CaO, MgO, and $TiO2$, we expect Na_2O to behave chemically similarly to K_2O because of similar alkali role in the melt (Thompson et al., 2007), and Naslund showed that CaO, MgO and $TiO2$ effects are minor for concentrations <1.5 wt%. Naslund showed that the average wt% differences between the two immiscible liquids increases with fO_2, with average wt% difference of FeO at T_{Liq} of 66, 53, 39, and 25 wt% for fO_2 of $10^{-0.7}$, 10^{-5}, 10^{-9} and 10^{-12}, respectively. Average FeO wt% difference of the two-phases present in amoeboids is 40 wt%, which falls between a fO_2 values of 10^{-5} and 10^{-9}. Thus, amoeboid compositions qualitatively reflect $fO_2 > 10 - 9$ (Fig. 5).

4.3. Amoeboid Record of Temperature History

L_{Fe} and L_{Si} compositions are also likely sensitive to their thermal histories due to the temperature-dependent width of the immiscibility dome. Lower equilibrium temperatures will result in more contrasting compositions. Uncertainties in the shape of multi-component silicate miscibility gaps and in the kinetics of LLPS make quantitative constraints difficult to distinguish from fO_2 effects. However, if we assume amoeboids experienced similar fO_2 environemnts during LLPS, variations in amoeboid composition will reflect different apparent equilibrium temperatures (T_{AE}), which has the potential to quantitatively constrain conditions as our knowledge of silicate LLPS thermodynamics and kinetics advances. Kamenetsky (Kamenetsky et al., 2013) shows an empirical connection for liquid immiscibility in a tholeiitic gabbro system between the T_{AE} using the distribution coefficients of SiO_2 between L_{Fe} and L_{Si} phases. Distribution coefficients between amoeboids vary from 0.36 to 0.47 (inset of Fig. 5), corresponding to differences in T_{AE} of 40 K in the Kamenetsky system. It is possible that, if fO_2 remains constant during LLPS, this variation in T_{AE} is related to variations in quench rates between amoeboids. For instance, while LLPS may rapidly result in stable liquid compositions at temperatures far above the liquidus, as amoeboids approach T_{Liq}, achievement of equilibrium may be kinetically limited and fail to reach the most contrasting equilibrium two-liquid compositions. Such limitations would result in compositions that reflect a T_{AE}, where $T_{AE} > T_{Liq}$. In this case, T_{AE} is a geospeedometry metric, where a higher T_{AE} reflects a faster quench rate for amoeboids of similar composition (Zhang et al., 1997). Important differences exist in the Kamenetsky system (which contains significant amounts of P_2O_5) that preclude quantitative T_{AE} in amoeboids, but the 40K variation in this metric shows that LLPS compositional variations of amoeboids preserved in fallout may be a result of some sensitivity to fireball thermal histories.

4.4. Iron Oxide Crystallization

After LLPS occurs, solidification of amoeboids and mm-scale glass occurs. Crystallization textures appear to be spatially confined, presumably to the original assumed liquid phase boundaries of amoeboid, such that average liquid phase compositions may be estimated using EDS raster measurements across each liquid phase region. While some L_{Fe} and L_{Si} regions formed during LLPS appear to solidify as single phases (Figs. 2G, 2J, 2R), usually these regions are a mixture of magnetite and glass (Fig. 3), which is consistent with quench textures of stable immiscible liquids reported by Naslund (Naslund, 1983). It is possible that liquid regions that quench into a single phase experienced faster quench rates, whereas regions that are a mixture of glass and magnetite crystals quenched slower, allowing diffusion-limited growth of crystalline phases to occur.

The overall level of crystaline growth observed in these samples is more prevalent than observations reported in previous studies, and is likely due to the significantly higher iron content present in these samples. Dendritic growth in iron-rich sample rims resemble quench crystals cooled at the fayalite/magnetite/quartz redox buffer (Isobe and Gondo, 2013) formed by rapid cooling 500 K/sec. This cooling rate is consistent with nuclear fireball cooling rates
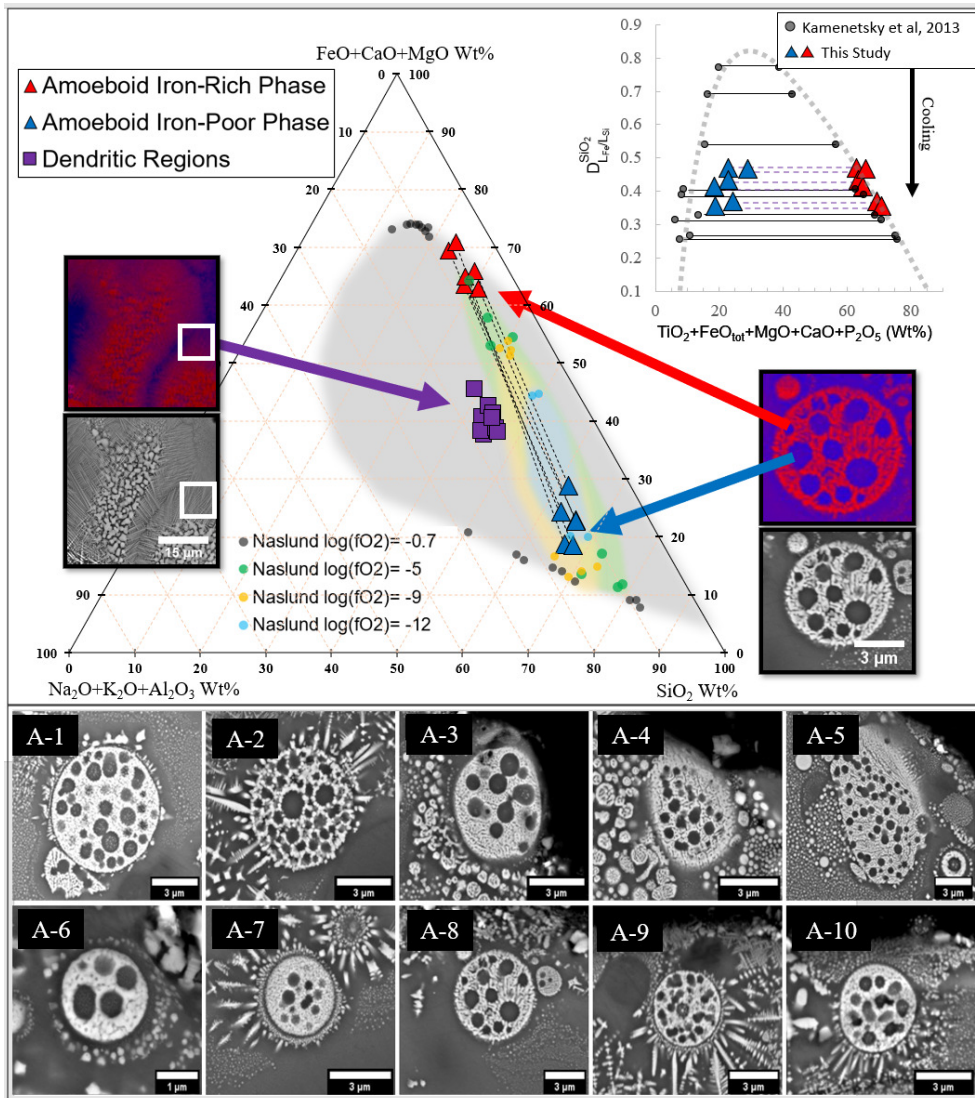
Figure 5: Oxygen fugacity and cooling rate interpretations of micro-structure compositions. Pseudo-ternary projection of amoeboid immiscibility pairs of amoeboids and dendrite compositions projected with immiscibility data at the liquidus temperatures for the $KAlSi_3O_8 - FeO - Fe_2O_3 - SiO_2$ system over a range of fO_2 (Naslund, 1983). Minor components may change the shape of the immiscibility region, but in general the relative difference in FeO reflects differences in fO_2. Suggested fields of immiscibility for a range of fO_2 based on the Naslund data is displayed as shaded areas. Only amoeboid with comparable aluminum content (within $1 - \sigma$ of the mean) are plotted due to immiscibility sensitivity to aluminum content. Thus, the plot shows only A-1, A-2, A-3, A-4, A-8, and A-9. Distribution coefficients (inset) of SiO_2 between immiscible amoeboid compositions reflect apparent equilibrium temperatures (T_{AE}) varying by up to 40 K (Kamenetsky et al., 2013), a proxy for quench rates.

estimated using luminosity measurements (Weisz et al., 2018; Klement, 1965), diffusion zoning (Weisz et al., 2018), and fission product decay chains (Cassata et al., 2014). While dendritic growth has been observed in some localized regions of trinitite glass (Eby et al., 2015; Bunch et al., 2012) and magnetite rims have recently been reported in some aerodynamic glassy fallout (Lukashenko et al., 2020), crystalline growth in fallout samples is relatively rare. Devitrification has been suggested as the genesis of magnetite structures recently reported by Lukashenko (Lukashenko et al., 2020), but no evidence for devitrification (Lofgren, 1971) is observed in the current sample suite. This work supports previous interpretations that non-equilibrium dendritic growth is the cause of magnetite rims in fallout (Bunch et al., 2012) rather than devitrification of iron-rich glass after formation (Lukashenko et al., 2020). TEM observations

of crystalline magnetite without the presence of hematite (α-Fe2O3) suggests only partially oxidized conditions were achieved, consistent with other recent observations (Cassata et al., 2014; Pacold et al., 2016) suggesting intermediate oxygen environments at the time of fallout formation.

4.5. Ex Situ (Amoeboid) vs. In Situ Immiscibility

Millimeter-scale fallout glass is primarily composed of entrained material that is not fully vaporized and does not reach thermal or chemical equilibrium with the fireball vapor (Weisz et al., 2018). As such, it is important to distinguish between processes that occurred within the mm-scale melt (*in situ*) and outside the mm-scale melt in micro-scale droplets of melt or condensate (*ex situ*) which are closer to equilibrium with the radioactive vapor. Many emulsion and interconnected textures in these samples, as well as the liquid immiscibiltiy textures reported previously (Bunch et al., 2012; Eby et al., 2015) represent *in situ* processes, and so reflect the local conditions present within the mm-scale melt rather than the vapor. While the elevated radioactivity and iron concentrations in regions of *in situ* immiscibility still suggest a significant vapor contribution, this vapor likely condensed and/or agglomerated at higher temperatures where it can dissolve and/or rapidly mix into the melt, obfuscating the record of the vapor environment prior to LLPS. In contrast, liquid immiscibility in objects formed *ex situ* (*i.e.* amoeboids) are more likely to maintain thermal and chemical equilibrium with the vapor, and for those that retain their formation morphologies after agglomeration onto and sub-summation into the host object, provide a new probe of the local vapor environment.

There is good textural and location evidence that many amoeboids reported in this study are formed *ex situ*. The near-rim location and degree of sphericity of most amoeboids, as well as surface-to-interior liquid flow textures (Fig. 2G) support an *ex situ* formation hypothesis. Their lack of gradations in size of nearby iron-rich spheres suggest agglomeration in contrast to *in situ* textures. Further, their sharp compositional boundaries with the the mm-scale host melt, spherical morphologies, and in some cases locations visible on the exterior of samples or only partial incorporation (Fig. 2E) support an *ex situ* formation hypothesis. In some amoeboids, halos of iron-rich crystallites or emulsion textures are present (Figs. 2F, 2G, 2J, 2M, 2N), suggesting some dissolution and mixing with the mm-scale host objects for some amoeboids. Their sizes are also consistent with previous records of particles formed during nuclear explosions that did not interact with the ground (<20 μm) (Nathans et al., 1970; Crocker et al., 1965), forming only from condensation and condensate agglomeration processes, with no mm-scale melts present to agglomerate onto.

4.6. Implications for Radionuclide Distributions

The frequent presence of both *in situ* and *ex situ* liquid immiscibility in these samples may have implications for radionuclide environmental mobility. There is uncertainty in the magnitude of such an effect since amoeboids are not a representative sampling of condensate particles. The LLPS process alters the chemistry and physical distribution of species within the particle while in the liquid state, including trace element partitioning between two immiscible silicate liquids (Ulff-Moller, 1998). In early times after a nuclear detonation, a significant portion of hazardous radioactivity is emitted from fission products which exist in similar trace concentrations within fallout glass. This suggests LLPS affects the distribution of hazardous radioactive species in the particle interiors (*i.e.* radioactive Cs-137 will partition into L_{Si} and Ba-140 will partition into L_{Fe} (Watson, 1976)). Radionuclides which partition into the less chemically durable L_{Fe} phase may have higher environmental mobility for fallout where such textures are present.

LLPS processes may also have implications for better understanding radiochemical fractionation processes historically observed in fallout, depending on what timeframe LLPS occurred during fireball cooling. Current models used for prediction of nuclear fallout formation (Norment, 1979) treat radiochemical fractionation semi-empirically and assume that all trace radioactive oxide species that condense prior to the solidification of the carrier material are distributed volumetrically throughout the μm-scale particles, and species that condense after solidification are distributed on the surface (Freiling, 1961; Miller, 1960). Other models attempt to account for kinetic condensation, diffusion, and re-evaporation effects, but suffer from a lack of experimental data (Norman and Winchell, 1966). If LLPS occurs while fission product mass chains are still condensing, the evolving composition of the amoeboid surface liquid may influence condensation process if there are kinetic limitations to condensation (*i.e.* liquid-vapor surface sticking coefficients (Norman and Winchell, 1966) or diffusion limitations (Weisz et al., 2018))and thus perturb particle size-dependent radiochemical fractionation patterns in μm-scale fallout particles. There is also uncertainty on how agglomeration processes influence radiochemical fractionation patterns in fallout particles (Freiling and Kay,

1966; Storebo, 1974). The immiscible nature of amoeboids reported here offer a new means to distinguish *in situ* vs. *ex situ* processes, which may increase our understanding of how agglomeration plays a role in fallout formation and radiochemical fractionation. While the effect of LLPS is limited to environments with compositions conducive to liquid immiscibility (i.e. iron-silicate), it warrants consideration in physics-based radiochemical fractionation and fallout contamination models that can be applied to a range of explosion geologies and environments.

5. Conclusion

Studies of immiscible silicate oxide systems allow inference of conditions during and following high-temperature LLPS not previously explored in nuclear fallout. In particular, *ex situ* amoeboid compositions sensitive to oxygen fugacity and quench rates provide a new means to understand high-temperature melts enriched in iron, with implications for radionuclide condensation, as well as expanding the compositional range of rapidly quenched silicate immiscibility systems observed in the meteorite impact melt and fulgurite literature. Crystallization of L_{Fe} regions offer further evidence for incompletely oxidized formation conditions and appear minimally complicated by potential weathering and low-temperature redox interactions in the decades since sample formation. Iron-rich amoeboid micro-structures observed in nuclear debris provide a new record of complex fireball system evolution with implications for incorporation of silicate immiscibility in future fallout fractionation and environmental contamination models.

References

Adams, C., Farlow, N., Schell, W., 1960. The compositions, structures and origins of radioactive fall-out particles. Geochimica et Cosmochimica Acta 18, 42 – 56. URL: http://www.sciencedirect.com/science/article/pii/0016703760900168, doi:https://doi.org/10.1016/0016-7037(60)90016-8.

Bellucci, J., Simonetti, A., 2012. Nuclear forensics: searching for nuclear device debris in trinitite-hosted inclusions. Journal of Radioanalytical and Nuclear Chemistry 293, 313–319.

Bonamici, C.E., Kinman, W.S., Fournelle, J.H., Zimmer, M.M., Pollington, A.D., Rector, K.D., 2017. A geochemical approach to constraining the formation of glassy fallout debris from nuclear tests. Contributions to Mineralogy and Petrology 172, 2.

Bunch, T.E., Hermes, R.E., Moore, A.M., Kennett, D.J., Weaver, J.C., Wittke, J.H., DeCarli, P.S., Bischoff, J.L., Hillman, G.C., Howard, G.A., et al., 2012. Very high-temperature impact melt products as evidence for cosmic airbursts and impacts 12,900 years ago. Proceedings of the National Academy of Sciences 109, E1903–E1912.

Cassata, W., Prussin, S., Knight, K., Hutcheon, I., Isselhardt, B., Renne, P., 2014. When the dust settles: stable xenon isotope constraints on the formation of nuclear fallout. Journal of environmental radioactivity 137, 88–95.

Crocker, G.R., O'Connor, J.D., Freiling, E.C., 1965. Physical and radiochemical properties of fallout particles. Technical Report. Naval Radiological Defense Lab., San Francisco, Calif.

Day, J.M., Moynier, F., Meshik, A.P., Pradivtseva, O.V., Petit, D.R., 2017. Evaporative fractionation of zinc during the first nuclear detonation. Science Advances 3, e1602668.

Ebert, M., Hecht, L., Hamann, C., Luther, R., 2017. Laser-induced melting experiments: Simulation of short-term high-temperature impact processes. Meteoritics & Planetary Science 52, 1475–1494.

Eby, G.N., Charnley, N., Pirrie, D., Hermes, R., Smoliga, J., Rollinson, G., 2015. Trinitite redux: Mineralogy and petrology. American Mineralogist 100, 427–441.

Eppich, G.R., Knight, K.B., Jacomb-Hood, T.W., Spriggs, G.D., Hutcheon, I.D., 2014. Constraints on fallout melt glass formation from a near-surface nuclear test. Journal of Radioanalytical and Nuclear Chemistry 302, 593–609.

Essene, E., Fisher, D., 1986. Lightning strike fusion: extreme reduction and metal-silicate liquid immiscibility. Science 234, 189–193.

Fleet, M., 1981. The structure of magnetite. Acta Crystallographica Section B: Structural Crystallography and Crystal Chemistry 37, 917–920.

Freiling, E.C., 1961. Radionuclide fractionation in bomb debris. Science 133, 1991–1998. URL: https://science.sciencemag.org/content/133/3469/1991, doi:10.1126/science.133.3469.1991, arXiv:https://science.sciencemag.org/content/133/3469/1991.full.pdf.

Freiling, E.C., Crocker, G.R., Adams, C.E., 1965. Nuclear debris formation, in: Radioactive fallout from nuclear weapons tests. Proceedings of an USAEC Conference. Washington, DC: US Atomic Energy Commission, pp. 1–41.

Freiling, E.C., Kay, M.A., 1966. Radionuclide fractionation in air-burst debris. Nature 209, 236–238.

Glass, B., Senftle, F., Muenow, D., Aggrey, K., Thorpe, A., 1987. Atomic bomb glass beads: Tektite and microtektite analogs, in: Proceedings of the Second International Conference on Natural Glasses, Charles University Prague. pp. 361–369.

Glasstone, S., Dolan, P.J., et al., 1977. The effects of nuclear weapons. volume 50. US Department of Defense.

Grieve, R.A., Pesonen, L.J., 1996. Terrestrial impact craters: their spatial and temporal distribution and impacting bodies, in: Worlds in Interaction: Small Bodies and Planets of the Solar System. Springer, pp. 357–376.

Hamann, C., Fazio, A., Ebert, M., Hecht, L., Wirth, R., Folco, L., Deutsch, A., Reimold, W.U., 2018. Silicate liquid immiscibility in impact melts. Meteoritics & Planetary Science 53, 1594–1632.

Hudon, P., Baker, D.R., 2002. The nature of phase separation in binary oxide melts and glasses. i. silicate systems. Journal of Non-Crystalline Solids 303, 299–345.

Isobe, H., Gondo, T., 2013. Dendritic magnetite crystals in rapid quenched fine spherules produced by falling experiments through the high temperature furnace with controlled gas flow. Journal of Mineralogical and Petrological Sciences 108, 227–237. doi:10.2465/jmps.121101.

Kamenetsky, V.S., Charlier, B., Zhitova, L., Sharygin, V., Davidson, P., Feig, S., 2013. Magma chamber–scale liquid immiscibility in the siberian traps represented by melt pools in native iron. Geology 41, 1091–1094.

Kersting, A., Efurd, D., Finnegan, D., Rokop, D., Smith, D., Thompson, J., 1999. Migration of plutonium in ground water at the nevada test site. Nature 397, 56–59.

Klement, A.W., 1965. Radioactive Fallout from Nuclear Weapons Tests: Proceedings of the Second Conference, Germantown, Maryland, November 3-6, 1964. Alfred W. Klement, Jr., Editor. 5, US Atomic Energy Commission.

Lewis, L., Knight, K., Matzel, J., Prussin, S., Zimmer, M., Kinman, W., Ryerson, F., Hutcheon, I., 2015. Spatially-resolved analyses of aerodynamic fallout from a uranium-fueled nuclear test. Journal of environmental radioactivity 148, 183–195.

Lofgren, G., 1971. Experimentally produced devitrification textures in natural rhyolitic glass. Geological Society of America Bulletin 82, 111–124.

Lukashenko, S., Kabdyrakova, A., Lind, O., Gorlachev, I., Kunduzbayeva, A., Kvochkina, T., Janssens, K., De Nolf, W., Yakovenko, Y., Salbu, B., 2020. Radioactive particles released from different sources in the semipalatinsk test site. Journal of Environmental Radioactivity 216, 106160. URL: http://www.sciencedirect.com/science/article/pii/S0265931X19304588, doi:https://doi.org/10.1016/j.jenvrad.2020.106160.

Miller, C., 1960. A theory of formation of fallout from land-surface nuclear detonations and decay of the fission products. Technical Report. NAVAL RADIOLOGICAL DEFENSE LAB SAN FRANCISCO CA.

Moerman, P.G., Hohenberg, P.C., Vanden-Eijnden, E., Brujic, J., 2018. Emulsion patterns in the wake of a liquid–liquid phase separation front. Proceedings of the National Academy of Sciences 115, 3599–3604.

Myers, J.t., Eugster, H., 1983. The system fe-si-o: Oxygen buffer calibrations to 1,500 k. Contributions to Mineralogy and Petrology 82, 75–90.

Naslund, H., 1983. The effect of oxygen fugacity on liquid immiscibility in iron-bearing silicate melts. American Journal of Science 283, 1034–1059.

Nathans, M.W., Thews, R., Holland, W.D., Benson, P.A., 1970. Particle size distribution in clouds from nuclear airbursts. Journal of Geophysical Research (1896-1977) 75, 7559–7572. URL: https://agupubs.onlinelibrary.wiley.com/doi/abs/10.1029/JC075i036p07559, doi:https://doi.org/10.1029/JC075i036p07559.

Norman, J., Winchell, P., 1966. Cloud chemistry of fallout formation.

Norment, H.G., 1979. DELFIC: Department of Defense Fallout Prediction System. Volume I-Fundamentals. Technical Report. ATMOSPHERIC SCIENCE ASSOCIATES BEDFORD MA.

Osinski, G., Grieve, R., Collins, G., Marion, C., Sylvester, P., 2008. The effect of target lithology on the products of impact melting. Meteoritics & Planetary Science 43, 1939–1954.

Osinski, G.R., 2003. Impact glasses in fallout suevites from the ries impact structure, germany: An analytical sem study. Meteoritics & Planetary Science 38, 1641–1667.

Pacold, J., Lukens, W., Booth, C., Shuh, D., Knight, K., Eppich, G., Holliday, K., 2016. Chemical speciation of u, fe, and pu in melt glass from nuclear weapons testing. Journal of Applied Physics 119, 195102.

Parsons-Davis, T., Knight, K., Fitzgerald, M., Stone, G., Caldeira, L., Ramon, C., Kristo, M., 2018. Application of modern autoradiography to nuclear forensic analysis. Forensic science international 286, 223–232.

Pasek, M.A., Pasek, V.D., 2018. The forensics of fulgurite formation. Mineralogy and Petrology 112, 185–198.

Roedder, E., 1978. Silicate liquid immiscibility in magmas and in the system k2o-feo-ai2o3-sio2: an example of serendipity. Geochimica et Cosmochimica Acta 42, 1597–1617.

Roedder, E., Weiblen, P.W., 1970. Silicate liquid immiscibility in lunar magmas, evidenced by melt inclusions in lunar rocks. Science 167, 641–644.

Shi, R., Wang, C., Wheeler, D., Liu, X., Wang, Y., 2013. Formation mechanisms of self-organized core/shell and core/shell/corona microstructures in liquid droplets of immiscible alloys. Acta materialia 61, 1229–1243.

Storebo, P.B., 1974. Formation of radioactivity size distributions in nuclear bomb debris. Journal of Aerosol Science 5, 557–577.

Storebö, P.B., 1960. Meteorological fractionation of nuclear bomb debris. Tellus 12, 293–297. URL: https://doi.org/10.3402/tellusa.v12i3.9400, doi:10.3402/tellusa.v12i3.9400.

Thompson, A.B., Aerts, M., Hack, A.C., 2007. Liquid immiscibility in silicate melts and related systems. Reviews in Mineralogy and Geochemistry 65, 99–127.

Ulff-Moller, F., 1998. Effects of liquid immiscibility on trace element fractionation in magmatic iron meteorites: A case study of group iiiab. Meteoritics & Planetary Science 33, 207–220.

Veksler, I.V., Dorfman, A.M., Borisov, A.A., Wirth, R., Dingwell, D.B., 2007. Liquid immiscibility and the evolution of basaltic magma. Journal of Petrology 48, 2187–2210.

Watson, E.B., 1976. Two-liquid partition coefficients: experimental data and geochemical implications. Contributions to Mineralogy and Petrology 56, 119–134.

Weber, W.J., Ewing, R.C., Angell, C.A., Arnold, G.W., Cormack, A.N., Delaye, J.M., Griscom, D.L., Hobbs, L.W., Navrotsky, A., Price, D.L., et al., 1997. Radiation effects in glasses used for immobilization of high-level waste and plutonium disposition. Journal of Materials Research 12, 1946–1978.

Weisz, D.G., Jacobsen, B., Marks, N.E., Knight, K.B., Isselhardt, B.H., Matzel, J.E., 2018. Diffusive mass transport in agglomerated glassy fallout from a near-surface nuclear test. Geochimica et Cosmochimica Acta 223, 377–388.

Zhang, Y., Jenkins, J., Xu, Z., 1997. Kinetics of the reaction h2o+ o→ 2 2oh in rhyolitic glasses upon cooling: Geospeedometry and comparison with glass transition. Geochimica et Cosmochimica Acta 61, 2167–2173.

A. Appendix

Table 1

L_{Si}-dispersed-in-L_{Fe} amoeboids in Sample F-10. Semi-quantitative bulk compositions represent EDS raster analysis across the cross section of the amoeboid, while L_{Fe} and L_{Si} compositions are estimated from ten point-analyses within each phase. EDS excitation volumes may have caused some mixing of compositions between phases, making 2-phase compositions more qualitative.

Wt%		SiO_2	FeO	Al_2O_3	K_2O	MgO	CaO	TiO_2	Na_2O
	Bulk	**42.37%**	**45.97%**	**6.33%**	**1.69%**	**1.17%**	**0.93%**	**0.81%**	**0.74%**
A-1	L_{Fe}	23.20%	67.20%	5.76%	0.96%	1.22%	0.72%	0.29%	0.66%
	L_{Si}	62.83%	21.32%	8.23%	3.66%	0.38%	1.08%	1.64%	0.86%
	Bulk	**46.98%**	**42.01%**	**5.71%**	**1.67%**	**1.36%**	**0.86%**	**0.74%**	**0.67%**
A-2	L_{Fe}	31.01%	58.96%	4.44%	1.19%	1.69%	0.38%	1.85%	0.49%
	L_{Si}	65.82%	19.23%	7.63%	2.86%	0.70%	1.62%	1.37%	0.77%
	Bulk	**40.68%**	**47.20%**	**6.85%**	**1.77%**	**1.32%**	**0.66%**	**0.72%**	**0.79%**
A-3	L_{Fe}	23.53%	68.32%	4.30%	0.75%	0.99%	0.63%	0.96%	0.53%
	L_{Si}	66.16%	16.60%	10.06%	3.46%	0.77%	0.78%	0.65%	1.53%
	Bulk	**39.41%**	**49.44%**	**6.21%**	**1.58%**	**1.06%**	**0.80%**	**0.81%**	**0.70%**
A-4	L_{Fe}	28.63%	59.72%	5.95%	1.68%	1.43%	1.09%	1.23%	0.28%
	L_{Si}	65.93%	19.61%	6.93%	3.57%	0.87%	1.02%	1.32%	0.75%
	Bulk	**39.45%**	**47.68%**	**7.63%**	**1.68%**	**1.26%**	**0.72%**	**0.82%**	**0.75%**
A-5	L_{Fe}	34.96%	54.97%	6.16%	1.14%	1.29%	0.28%	0.50%	0.70%
	L_{Si}	67.19%	15.32%	10.22%	2.76%	1.05%	1.55%	0.77%	1.14%
	Bulk	**39.36%**	**49.86%**	**4.70%**	**1.60%**	**1.34%**	**0.99%**	**1.21%**	**0.94%**
A-6	L_{Fe}	23.28%	66.46%	4.52%	0.71%	2.58%	0.45%	1.57%	0.43%
	L_{Si}	51.56%	35.99%	7.52%	1.66%	0.87%	0.73%	0.22%	1.45%
	Bulk	**31.29%**	**55.90%**	**7.63%**	**1.53%**	**1.79%**	**0.72%**	**0.64%**	**0.50%**
A-7	L_{Fe}	27.58%	60.78%	7.02%	1.49%	2.25%	0.22%	0.56%	0.10%
	L_{Si}	46.04%	38.43%	9.47%	2.89%	1.15%	1.14%	0.49%	0.40%
	Bulk	**42.18%**	**45.52%**	**6.61%**	**2.12%**	**1.36%**	**0.93%**	**0.61%**	**0.68%**
A-8	L_{Fe}	27.92%	61.46%	5.42%	1.18%	2.32%	0.75%	0.41%	0.54%
	L_{Si}	67.55%	14.93%	9.08%	3.63%	0.55%	1.89%	1.20%	1.18%
	Bulk	**43.79%**	**45.49%**	**5.15%**	**1.81%**	**1.62%**	**0.79%**	**0.73%**	**0.61%**
A-9	L_{Fe}	28.87%	62.82%	3.47%	1.32%	1.88%	0.67%	0.61%	0.36%
	L_{Si}	61.80%	25.55%	5.88%	2.61%	1.17%	1.26%	0.85%	0.89%
	Bulk	**36.31%**	**54.89%**	**4.53%**	**1.27%**	**1.23%**	**0.62%**	**0.59%**	**0.57%**
A-10	L_{Fe}	20.56%	72.44%	3.54%	0.37%	2.28%	0.38%	0.22%	0.21%
	L_{Si}	58.57%	30.01%	5.92%	2.45%	0.64%	0.76%	0.58%	1.08%
Amoeboid Avg		**40.18%**	**48.40%**	**6.13%**	**1.67%**	**1.35%**	**0.80%**	**0.77%**	**0.70%**
1-σ		4.27%	4.31%	1.11%	0.22%	0.21%	0.12%	0.18%	0.12%
L_{Fe} Avg		**26.95%**	**63.31%**	**5.06%**	**1.08%**	**1.79%**	**0.56%**	**0.82%**	**0.43%**
1-σ		4.33%	5.22%	1.18%	0.39%	0.55%	0.26%	0.56%	0.19%
L_{Si} Avg		**61.35%**	**23.70%**	**8.09%**	**2.95%**	**0.82%**	**1.18%**	**0.91%**	**1.00%**
1-σ		7.28%	8.51%	1.59%	0.64%	0.26%	0.40%	0.45%	0.34%